Anisotropic mesh adaptation with optimal convergence for finite elements using embedded geometries

Dieu-Linh Quan[1], Thomas Toulorge, Emilie Marchandise, Jean-François Remacle, Gaëtan Bricteux

Université catholique de Louvain, Institute of Mechanics, Materials and Civil Engineering (iMMC), Place du Levant 1, 1348 Louvain-la-Neuve, Belgium

Abstract

This paper presents a numerical study of a recent technique that consists in modeling embedded geometries by a level-set representation in combination with local anisotropic mesh refinement. The local anisotropic mesh procedure is suitable for various orders p of finite element approximations. This method proves beneficial in simulations involving complex geometries, as it suppresses the need for the tedious process of body-fitted mesh generation, without altering the finite element formulation nor the prescription of boundary conditions. The first part of the study deals with a simple Laplace problem featuring a planar interface on which a Dirichlet boundary condition is imposed. It is shown that the appropriate amount of local isotropic refinement yields the optimal convergence rate for various finite element orders p, unlike uniform refinement. Anisotropic refinement further ensures geometric convergence and limits the growth of the number of unknowns. Then, we explain how to use metric-based anisotropic adaptation to obtain *nearly* body-fitted meshes with arbitrary geometries. The optimal rate of convergence, both for the solution and the geometry, is demonstrated on 2D and 3D academic Laplace problems involving curved boundaries. Finally, applications in the field of fluid dynamics and material science are presented. The results for these simulations successfully converge towards data from the literature, analytical solutions or values obtained with body-fitted meshes.

Keywords: anisotropic mesh, adaptive refinement, embedded Dirichlet,

[1]Corresponding author. Tel.: +3210472362; Fax: +3210472180.
E-mail address: dieulinh.quan@uclouvain.be

level-set, embedded interface, error estimate, optimal convergence rate, elliptic equation

1. Introduction

In the context of computational fluid and solid mechanics, numerical methods are applied to increasingly challenging problems that often involve complex geometries. The usual strategy to handle such cases is to firstly generate an unstructured mesh which conforms to the geometry, and then solve the physical problem with a numerical method that works with unstructured meshes, such as the Finite Element Method (FEM). However, most meshing software packages rely on a high-quality CAD description of the domain geometry, which is not readily available in the traditional workflow of professionals in sectors like architecture [11]. In the field of medicine, the quality of the primary CAD models obtained through imaging techniques may not be sufficient to allow direct meshing [24]. If the geometry evolves in time, the mesh is usually modified during the simulation, either by deformation techniques relying on elastic analogies, which sometimes lacks robustness, or by complete remeshing, which is computationally expensive.

Similar issues, that arise in multi-physics problems involving moving interfaces, have fostered research efforts to embed the description of the geometry in the formulation of the numerical method. In this way, the meshing work needed to take into account complex features such as cracks and material interfaces can be dramatically reduced. Moreover, this removes the need for high-quality CAD data, as no topological information on the geometry is then required in the meshing process.

In the immersed boundary method [30], fluid-solid interfaces are modeled from a Lagrangian point of view as a set of discrete force generators. Other approaches retain an Eulerian description consistent with the underlying numerical method by relying on the advection of interface-tracking quantities. Among them, the Marker-and-Cell [27] and the Volume of Fluid methods [1] make use of "marker" quantities that require a specific numerical treatment because of their discontinuous character. A more convenient continuous representation of the interface can be obtained through level-set functions [7, 26]. Level-set techniques have also been used recently to model fixed, but complex boundaries in an immersed volume framework [20].

While level-set curves and other types of interface-tracking functions are an efficient solution for representing geometries embedded in non-fitted

meshes, they make it more difficult to impose boundary conditions. Indeed, they prevent nodal collocation, which makes the prescription of Dirichlet conditions particularly challenging. To deal with this problem, some approaches based on penalty methods or Lagrange multipliers have been proposed in the literature [13, 21]. The issue of Babuška-Brezzi stability has been addressed using either stable [4] or stabilized [3, 14] approaches, that have drawbacks. The stable method presented in [4] is relatively complex, as it requires the definition of a specific set of Lagrange multipliers that depend on the topology of the mesh. Stabilized methods are more standard with respect to the finite element technology, but choosing appropriate values for the parameters that control the stabilization may not be obvious. More importantly, both approaches are intrusive in the sense that they require deep modifications in finite element kernels, either by introducing new finite element unknowns [29] or by modifying standard finite element formulations (or both).

In this paper, we follow another approach that relies on local anisotropic mesh adaption [7, 2, 12] around the geometry to obtain *nearly* body-fitted meshes, which combines the benefits of the aforementioned methods:

1. The Dirichlet boundary condition is imposed in a strong manner by nodal collocation, just as with body-fitted meshes,

2. The standard finite element formulation is used as is, without resorting to basis enrichment or Lagrange multipliers that alter its numerical properties,

3. The mesh does not conform exactly to the embedded geometry, which facilitates the meshing process and makes it possible to use level-set functions instead of high-quality CAD data.

Because anisotropic mesh adaption procedures have gained in robustness and availability in the last decade, this approach has become competitive with respect to the modification of finite element formulations. The aim of this paper is to show that optimal convergence rates can be easily obtained using the standard finite element discretization of the variational weak form, with barely the same number of degrees of freedom as in a conforming mesh approach and without changing the finite element formulation. Both two- and three-dimensional examples illustrate the new approach.

The paper is organized as follows. The next section 2 gives an overview of the adaptive strategy. Section 3 involves two-dimensional examples while

numerical results for three-dimensional cases are discussed in section 4. We show applications of this approach in section 5 and draw conclusions in section 6.

2. Optimal *nearly* body-fitted meshes

Our technique for imposing Dirichlet boundary conditions on embedded surfaces relies on the generation of an anisotropic adaptive mesh for which the mesh size is carefully chosen in order to ensure the optimal convergence of both the solution and the geometry of the interface.

2.1. General principle

Let M be a mesh of a domain Ω that is composed of n_e elements $e_i,\ i = 1, \ldots, n_e$ and n_v vertices $\mathbf{x}_i,\ i = 1, \ldots, n_v$. Consider an embedded interface Γ (see Figure 1) that can be modeled by the iso-zero value of a level-set function $\phi(\mathbf{x})$. The level-set function is then defined in all the domain as the signed distance to the interface.

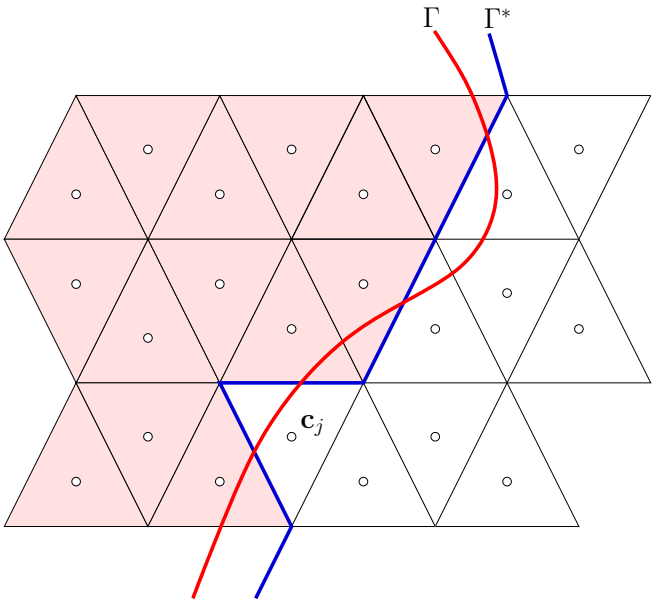

Figure 1: A triangular mesh with the iso-zero of a levelset Γ. Stair-cased curve Γ^* is the discrete version of Γ. Round dots represent centroids of triangles.

In practice, the level-set function $\phi(\mathbf{x})$ is evaluated at the center of gravity $\mathbf{c}_i$ of every element e_i. The sign of $\phi(\mathbf{c}_i)$ determines whether element e_i is either on one side or on the other side of the levelset. On Figure 1, colored elements correspond to $\phi(\mathbf{c}_i) > 0$ and non-colored elements correspond to $\phi(\mathbf{c}_i) < 0$. Mesh edges that separate colored and non colored elements constitute the discrete approximation Γ^* of the continuous interface Γ.

This way of treating the interface has obvious advantages. No enrichment is needed to account for intra-element features, as it is the case in X-FEM. Standard finite element formulations can therefore be used as is for solving a problem with an embedded interface. Yet, it is well known that this treatment of interfaces leads to a poor first order of convergence in finite element simulations [28]. In this paper, we address this issue using anisotropic mesh adaptation near the interface Γ. The fact that mesh generators and finite element solvers are independent software components makes this approach appealing in practice.

2.2. Need for adaptive mesh refinement

Assume a mesh of elements with sizes h_{e_i}, $i = 1, \ldots, n_e$ and an associated finite element solution at order p, u_h, that is an approximation of the smooth exact solution u. The L_2 error on element e_i is of order:

$$\epsilon_i = \sqrt{\int_{e_i} \|u - u_h\|^2 d\mathbf{x}} = \mathcal{O}\left(h_{e_i}^k\right) \tag{1}$$

with $k = p + 1$ in smooth regions and $k = 1$ in the vicinity of the interface.

We first study the simple one-sided 2D Laplace problem [13]:

$$\begin{aligned}
\Delta u &= 0, && \text{in } \Omega^+ : [0,1] \times [y^*, 1] && (2)\\
u &= \sin(\pi x)\hat{v}(y^*), && \text{at } \Gamma \ : y = y^* = 1/3 && (3)\\
u &= 0, && \text{at } \Gamma_D : y = 1 && (4)\\
\nabla u \cdot \mathbf{n} &= -\pi \hat{v}(y), && \text{at } \Gamma_N : x = 0;\ x = 1 \text{ and } y^* < y < 1 && (5)
\end{aligned}$$

The known analytical solution is $u(x, y) = \sin(\pi x)\hat{v}(y)$ where $\hat{v}(y) = \cosh(\pi y) - \coth(\pi)\sinh(\pi y)$.

The embedded planar surface Γ splits the domain $\Omega = [0, 1] \times [0, 1]$ into two parts Ω^+ and Ω^-. As discussed, the Dirichlet boundary condition on Γ is prescribed by imposing the value $\sin(\pi x)\hat{v}(y^*)$ at the nodes defining the discrete approximation Γ^* to Γ.

We perform a convergence study consisting in refining uniformly the mesh and measuring the global L_2 discretization error in the domain:

$$\mathcal{E}_{L_2}(u) = \sqrt{\sum_i \epsilon_i^2}. \tag{6}$$

Let us define a mesh refinement factor $r > 1$ and a refinement level l that determine for a *uniform mesh refinement* the mesh element size h as:

$$h^l = \frac{h_0}{r^l}, \quad l = 1, ..., l_n \tag{7}$$

where h_0 is an initial uniform mesh element size and l_n is the number of refinement levels. In this case, we solve Equation (2) using linear finite elements ($p = 1$) on a sequence of five progressively uniform isotropic refined meshes ($l_n = 5$) with an initial mesh size of $h_0 = 0.1$ and a refinement factor of $r(\mathbf{x}) = 2$ (see Figure 2). In this way, each linear triangular element is divided into four congruent triangles of half size and the new vertices of new elements lie exactly at the midpoint of the parent element's edges.

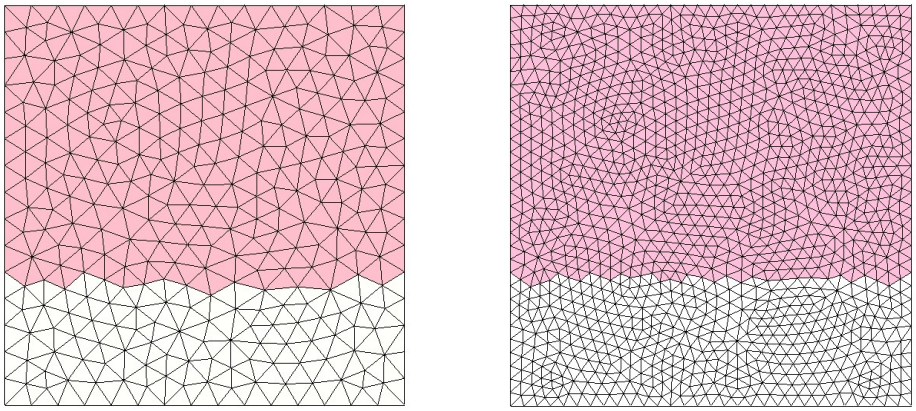

(a) Initial isotropic mesh (b) Uniformly refined mesh

Figure 2: Coarsest isotropic mesh ($h_0 = 0.1$) and isotropic uniform refined one ($p = 1$ and $r = 2$) for the one-sided Problem (2).

The results of the convergence study are shown in Figure 4, demonstrating a linear rate of convergence with uniform refinement, while the finite element

method should yield second-order convergence for smooth problems.

It is thus clear that the poor first order rate of convergence shown for uniform refinement is due to the loss of accuracy at the interface. However, it is possible to obtain the optimal convergence by setting the mesh refinement factor $r(\mathbf{x})$ differently depending on whether an element is close to the embedded interface Γ or not. Indeed, as we have $\epsilon_i = \mathcal{O}(h_{e_i})$ near the interface and $\epsilon_i = \mathcal{O}(h_{e_i}^{p+1})$ in the bulk region, a global convergence order of $p+1$ can only be obtained if the refinement factor close to the interface is chosen as

$$r_\Gamma = r_b^{p+1} \Rightarrow h_\Gamma = \frac{h_0}{r_\Gamma}. \tag{8}$$

where r_b denotes the refinement factor in the bulk region. This means that the gap between the interface Γ and its nearly body-fitted version Γ^* has to decrease more rapidly than the bulk element size to ensure an optimal global rate of convergence. An example of a mesh refined with isotropic adaptation for the 2D Laplace problem is shown in Figure 3. In practice,

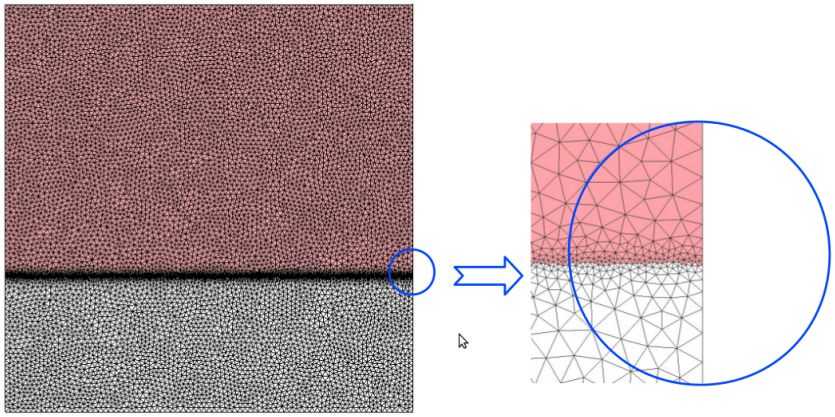

Figure 3: Isotropic adaptive refined mesh for the 2D Laplace problem (2) for linear finite elements ($p = 1, h_0 = 0.1, r = r_b = 2, l = 4, E = 0.1$).

mesh adaptation is performed in the vicinity of the iso-zero of $\phi(\mathbf{x})$, i.e. in a band $\{\mathbf{x} \text{ s.t. } |\phi(\mathbf{x})| \leq E\}$ of thickness $2E$ around the interface. The mesh size for *isotropic adaptive mesh refinement* is computed by linearly interpolating between the minimal value $h_\Gamma^l = h_0/(r_\Gamma)^l$ at the interface Γ and a maximal

value of $h_b^l = h_0/(r_b)^l$ in the bulk region:

$$h^l(\mathbf{x}) = h_\Gamma^l + \frac{h_b^l - h_\Gamma^l}{E}|\phi(\mathbf{x})|. \tag{9}$$

Here, r_b is a constant refinement factor in the bulk region.

Convergence results for the adaptive isotropic mesh refinement are shown in Figure 4. It can be clearly seen that the optimal second-order convergence rate is recovered when applying isotropic adaptive refinement technique.

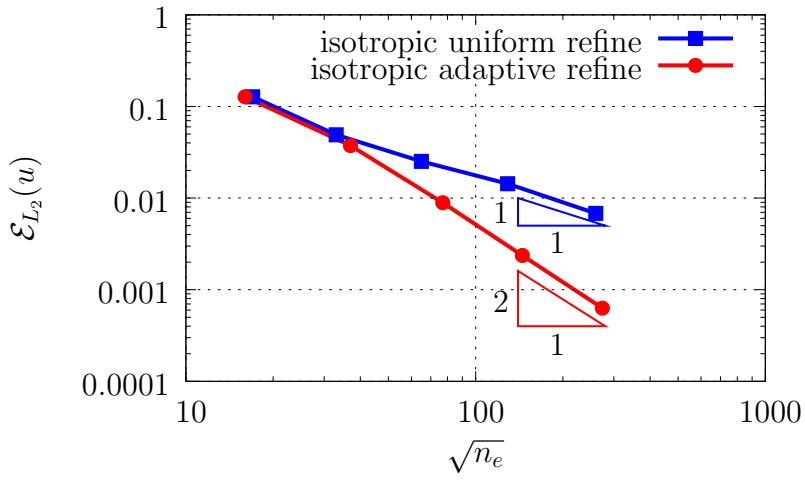

Figure 4: Convergence study for the 2D Laplace problem (2)-(5): comparison between isotropic uniform and isotropic adaptive refinement techniques.

2.3. Need for anisotropic mesh refinement

Although the isotropic mesh refinement procedure provides the optimal convergence rate for the solution, it suffers from two problems: it does not enable geometrical convergence, and it still involves a significantly higher number of elements than body-fitted meshes.

First, the discrete representation Γ^* of the exact interface Γ is stair-cased even when employing very fine elements (see Figure 3), so Γ^* does not converge uniformly towards Γ. More specifically, the measure of the interface (length in 2D or surface in 3D) does not converge to its exact value. This can be seen in Figure 5 where the L_1 geometric error $\mathcal{E}_{geo}$, which is defined

in Eq. 10 and is measured as the error in the length of the interface, remains at a quasi constant level for isotropic adaptive refinement.

$$\mathcal{E}_{geo} = \|l_{\Gamma *} - l_{\Gamma}\| \tag{10}$$

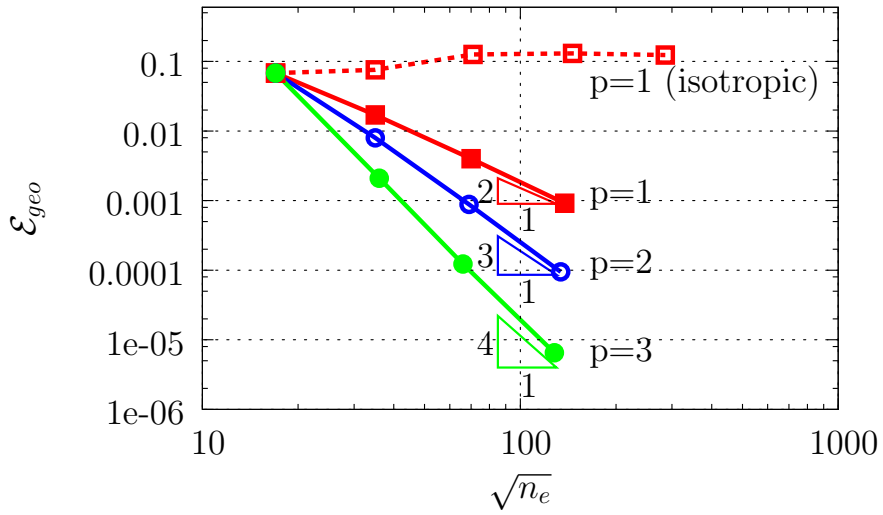

Figure 5: Geometric error for the interface Γ_* of problem (2)-(5) analysis using high-order elements and anisotropic adaptive refinement technique. Comparison with the isotropic uniform refinement for $p = 1$.

Such methods are thus severely limited when quantities of interest are integral values over the interface. In a CFD computation, for instance, it would lead to a large error in the evaluation of the lift and drag forces applied to the geometry by the flow. In a crack propagation simulation, the propagation path and velocity, that depend on quantities integrated along the crack line, would be strongly mispredicted.

Moreover, the isotropic mesh refinement implies a rapid growth in the number of elements in the band of thickness $2E$ around the interface. Even if the band is narrow compared to the size of the entire computational domain, this growth can lead to a significant increase in the global number of degrees of freedom, which affects negatively the computational cost. A comparison of the number of elements n_e and the number of vertices n_v between uniform refined meshes and isotropic adaptive refined meshes for Problem 2 is shown

l	h^l	n_e^{uniform}	h_Γ^l	$n_e^{\text{isoAdaptive}}$	$\Delta n_e(\%)$
1	0.1	275	0.1	275	0
2	0.05	1057	0.025	1402	32.64
3	0.025	4227	0.00625	5890	39.34
4	0.0125	16767	0.00156	20967	25.05
5	0.00625	67725	0.00039	75277	11.15

Table 1: Mesh sizes and number of elements in refined meshes with isotropic uniform and isotropic adaptive refinement techniques for Problem (2)-(5). We have $h_0 = 0.1, p = 1$ and $r = r_b = 2$ so that $r_\Gamma = 4$ and $h^l = h_b^l$.

in Table 1. Both refinement techniques started from an initial uniform mesh at the coarsest level corresponding to $h_0 = 0.1$. The uniform refinement factor and the bulk refinement factor are equal: $r = r_b = 2$ so that the refined meshes have the same mesh size $h^l = h_b^l$ in the bulk region for both refinement techniques. An average overhead of $\Delta n_e = 27.05\%$ in the number of elements n_e is observed for adaptively refined meshes compared to their uniformly refined counterparts.

A solution to both problems is to interpret r_Γ in Formula (8) as a mesh refinement factor that should be applied only in the orthogonal (or normal) direction to the level-set, so that only the mesh edges that cross the interface become very small. In the tangential direction, using a lower refinement factor should still yield the optimal rate of global convergence, as the solution along the interface is smooth.

In the case of the planar interface of Problem 2, the refinement factor in the tangential direction can be the same as in the bulk region. However, in the more general case of a curved boundary, the error on the solution in the vicinity of the interface results both from the finite element approximation and from the approximate representation of the geometry. Elements that are used in mesh generation are geometrically linear (i.e. straight sided), so the geometrical approximation, measured by the "gap" between the approximate and exact interfaces, converges at a second-order rate. Here, we assume that the part of the error in the solution that is due to the geometrical approximation decreases at the same rate as the geometrical error. The

mesh refinement factor tangential to the interface is then computed as:

$$r_t = r_b^{(p+1)/2}. \tag{11}$$

Tangential mesh sizes are then also interpolated linearly in the band of thickness E.

In this manner, the geometry of the numerical approximation Γ^* of the interface Γ converges to the exact one. As seen in Figure 6, the elements in the vicinity of the interface become increasingly stretched along Γ, which effectively controls the measure of Γ^*, preventing it from becoming "fractal-like" in the refinement process. We analyze the error in the 2D Laplace problem (2), using the proposed approach, with elements of different polynomial orders ($p = 1, 2, 3$). All the cases start with the same isotropic initial mesh ($h_0 = 0.1$). The refinement factors are $r_b = 2$ in the bulk region away from the interface and $r_\Gamma = 2^{p+1}$ in the fine region close to the interface. While the geometric error using isotropic mesh refinement does not decrease at all, the results of adaptive anisotropic refinement plotted in Figure 5 show the advantage of this technique in terms of geometric convergence.

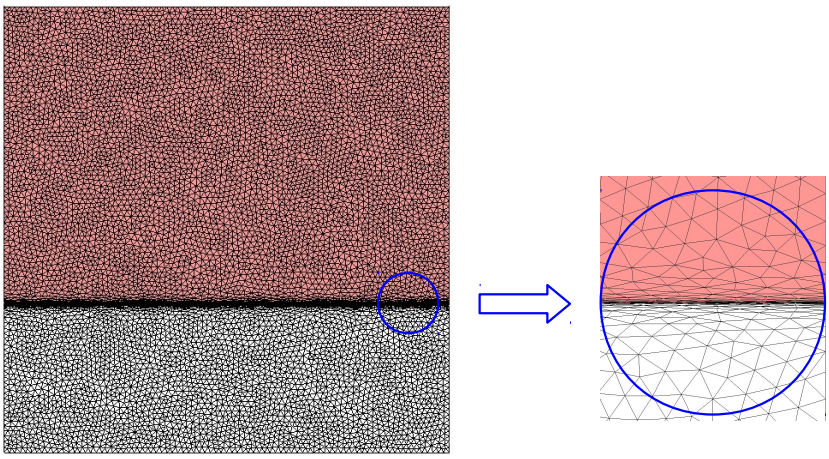

Figure 6: Anisotropic adaptive refined mesh for the 2D Laplace problem (2)-(5): $p = 1, r = 2$ so that $r_\Gamma = 4$ and $r_t = 2$.

Moreover, the growth of the number of nodes in the mesh remains limited. The first 2D example presented in Section 3 (see Figure 11) shows that an increase of only 17.8% in number of vertices with respect to uniformly

refined meshes is sufficient for obtaining optimal convergence, even though the interface is much longer than in Problem 2.

2.4. Mesh metric field construction in anisotropic adaptivity technique

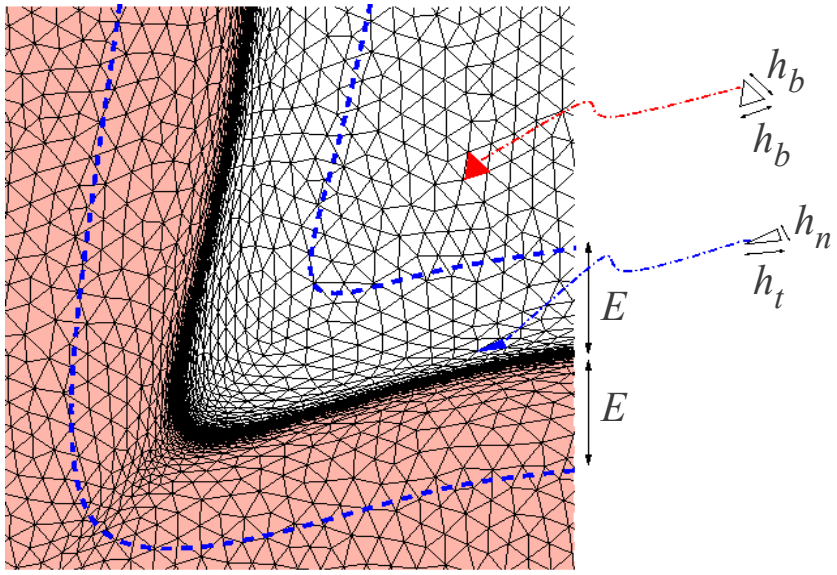

Figure 7: Illustration for mesh size definition (h_n, h_t and h_b) in 2D anisotropic adaptive mesh

There exist open source mesh generators that allow to generate anisotropically adapted meshes based on metric maps, e.g. BAMG [22] in 2D and MMG3D [10] in 3D. Mesh adaptation in BAMG is based on a global constrained Delaunay kernel, while local mesh modifications are applied in MMG3D.

The aim of metric-based anisotropic mesh adaptation is to generate a uniform unit mesh [16] in a prescribed Riemannian metric space, in order to obtain an anisotropic adapted mesh in the Euclidean space. Anisotropic mesh adaptation is performed in the vicinity of the interface Γ described by the level-set function $\phi(\mathbf{x})$, i.e. in a band $\{\mathbf{x} \text{ s.t. } |\phi(\mathbf{x})| \leq E\}$ of thickness $2E$ around Γ.

With a linear discretization, the approximation error on the level-set function $\phi(\mathbf{x})$ is of second order. An appropriate metric field $\mathcal{M}$ can thus be constructed from the gradient vector $\nabla\phi(\mathbf{x}) = (\phi_x\ \phi_y\ \phi_z)^T$ and the Hessian

matrix $\mathcal{H}(\phi(\mathbf{x}))$ of $\phi(\mathbf{x})$:

$$\mathcal{H}\left(\phi(\mathbf{x})\right) = \begin{pmatrix} \phi_{xx} & \phi_{xy} & \phi_{xz} \\ \phi_{yx} & \phi_{yy} & \phi_{yz} \\ \phi_{zx} & \phi_{zy} & \phi_{zz} \end{pmatrix} \tag{12}$$

Let us define an orthogonal basis $R^3 = \{\mathbf{n}, \mathbf{t}_1, \mathbf{t}_2\}$ at any point of the interface Γ, with $\mathbf{n}$ the unit normal vector to the interface and $\mathbf{t}_1, \mathbf{t}_2$ two unit tangent vectors in the principal directions of curvature of the surface defined by the iso-zero of the levelset. At any point in the band of thickness $2E$ around Γ, the Hessian matrix can undergo an eigenvalue decomposition:

$$\mathcal{H}\left(\phi(\mathbf{x})\right) = R^T \begin{pmatrix} \lambda_n & 0 & 0 \\ 0 & \lambda_{t_1} & 0 \\ 0 & 0 & \lambda_{t_2} \end{pmatrix} R. \tag{13}$$

If $\phi(\mathbf{x})$ is a distance function, the eigenvectors corresponding to the eigenvalues λ_n, λ_{t_1} and λ_{t_2} are proportional to $\mathbf{n}$, $\mathbf{t}_1$ and $\mathbf{t}_2$ respectively. Assuming that $h_n(\mathbf{x})$, $h_{t_1}(\mathbf{x})$ and $h_{t_2}(\mathbf{x})$ denote the element edge lengths in three principal directions (see in Figure 7 for a detail illustration of notations), λ_n, λ_{t_1} and λ_{t_2} shall be inversely proportional to $h_n^2(\mathbf{x})$, $h_{t_1}^2(\mathbf{x})$ and $h_{t_2}^2(\mathbf{x})$, respectively.

In practice, the construction of the metric $\mathcal{M}$ at a given point of the band of thickness $2E$ around Γ requires thus the definition of the element edge lengths and the determination of the corresponding directions.

The normal direction $\mathbf{n}$ is obtained directly from the gradient $\nabla\phi(\mathbf{x})$. The associated element size h_n is computed by linearly interpolating between the minimal value $h_{n\Gamma}$ of elements located on the interface Γ and the maximal value h_b of isotropic elements in the bulk region:

$$h_n(\mathbf{x}) = h_{n\Gamma} + \frac{h_b - h_{n\Gamma}}{E} \left|\phi(\mathbf{x})\right|. \tag{14}$$

In the tangential directions $\mathbf{t_i}$ ($i = 1, 2$ for a general 3D case), the mesh size h_{t_i} is determined as:

$$h_{t_i} = \frac{2\pi}{\kappa_i N_p}, \tag{15}$$

where N_p is a user-specified parameter that represents the number of mesh points needed to discretize a whole circle and κ_i are principal curvatures

corresponding to two directions $\mathbf{t}_i$. For two dimensional cases, the unique tangential direction is directly obtained as $\mathbf{t} = (-\phi_y \ \phi_x)^T$, and the curvature formula for implicit planar curves is given by [19]:

$$\kappa = \frac{\left|\mathbf{t}^T \mathcal{H}\, \mathbf{t}\right|}{|\nabla\phi(\mathbf{x})|^3} \tag{16}$$

For 3D cases, the gradient $\nabla\mathbf{n}$ of the unit normal vector $\mathbf{n}$ to the implicit embedded surface $\phi(\mathbf{x}) = 0$ is given by [5]:

$$\nabla\mathbf{n} = -\frac{1}{|\nabla\phi(\mathbf{x})|}\left(\mathcal{I} - \mathbf{n}\cdot\mathbf{n}^T\right)\mathcal{H}(\phi(\mathbf{x})) \tag{17}$$

where $\mathcal{I}$ is the identity matrix. The two non-zero eigenvalues of $\nabla\mathbf{n}$ give the two principal curvatures κ_i, and the corresponding directions $\mathbf{t}_i$ are the associated eigenvectors [5]. The formula can further be simplified for a distance function $\phi(\mathbf{x})$, as then $|\nabla\phi(\mathbf{x})| = 1$.

In practice, it is necessary to truncate the small and the large eigenvalues by imposing the maximal size as h_b and the minimal size as $h_{n\Gamma}$ in order to avoid singular metric case and to limit the local density of the adapted mesh [2]. Modified eigenvalues are then defined by:

$$\lambda'_n = \min\left(\max\left(\lambda_n, \frac{1}{h_b^2}\right), \frac{1}{h_{n\Gamma}^2}\right) \tag{18}$$

$$\lambda'_{t_i} = \min\left(\max\left(\lambda_{t_i}, \frac{1}{h_b^2}\right), \frac{1}{h_{n\Gamma}^2}\right) \tag{19}$$

The anisotropic mesh metric can finally be computed as:

$$\mathcal{M}(\mathbf{x}) = R'^T \begin{pmatrix} \lambda'_n & 0 & 0 \\ 0 & \lambda'_{t_1} & 0 \\ 0 & 0 & \lambda'_{t_2} \end{pmatrix} R', \tag{20}$$

where the matrix R' is made up of $\mathbf{n}$, $\mathbf{t}_1$ and $\mathbf{t}_2$. It is clear that the three unit vectors in the basis R^3 prescribe the orientation while the λ'_n, λ'_{t_1} and λ'_{t_2} control the size of the mesh elements along these directions. The meshing procedure gets the directional information of element shape and size from the metric tensor field $\mathcal{M}(\mathbf{x})$ and generates an adapted mesh. In the bulk region outside the transition band, the isotropic mesh is generated by prescribing

an isotropic metric corresponding to a uniform mesh size h_b.

In the next sections, series of refined meshes will be generated for different cases using the proposed technique. Three parameters are given as input of the mesh adaptation procedure: the width E of the transition band, the mesh size $h_{n\Gamma}$ in the normal direction at the interface, and the mesh size h_b in the bulk region. For all cases, the relations between the given mesh sizes for each each refinement level l and the initial mesh ($l = 0$) are given by:

$$h_b^l = \frac{h_b^0}{r_b^l} \quad \text{and} \quad h_{n\Gamma} = \frac{h_{n\Gamma}^0}{r_{n\Gamma}^l}, \; r_{n\Gamma} = r_b^{p+1}. \tag{21}$$

3. Curved interface embedded in square domain

A complex two-dimensional curved interface of flower-like shape with high curvature is embedded in a square domain $\Omega = [-1, 1] \times [-1, 1]$. This kind of geometry is a typical of irregular interfaces. It is therefore appropriate for evaluating the accuracy of methods designed to solve elliptic problems, see e.g. [14, 23, 18]. The level-set defining the curved interface in polar coordinates is:

$$\phi(r, \theta) = r - 0.3 - 0.05 \sin(6\theta), \quad \text{with} \quad \theta \in [0, 2\pi] \tag{22}$$

and the Poisson equation $\Delta u = 4$ with the exact solution $u = x^2 + y^2$ (Figure 8) is taken into consideration.

The only boundary of the computational domain is the embedded interface. The Dirichlet boundary condition imposed at each point $P^*(r^*, \theta^*)$ on Γ^* is determined based on the exact solution, i.e. $u = r^2$ taken at the corresponding point $P(r, \theta)$ on the exact surface Γ. In this case P can be determined simply as the intersection point of OP^* and the exact surface Γ; therefore, P and P^* have the same coordinate $\theta = \theta^*$ while the second polar coordinate r can be calculated from the level-set equation as $r = 0.3 + 0.05 \sin(6\theta^*)$.

We first solve the problem using linear finite elements ($p = 1$) on two sequences of five progressively refined meshes ($l = 1, \ldots, 5$). In both cases, we start from the same initial isotropic mesh $h_0 = h_b^0 = 0.1$, and the bulk refinement factor is set to $r_b = 2$. The first sequence corresponds to the isotropic uniform refinement governed by Equation (7). The other one (see Figure 9) is obtained through anisotropic adaptive refinement, the mesh sizes being given by Equation (21) with $r_{n\Gamma} = 4$.

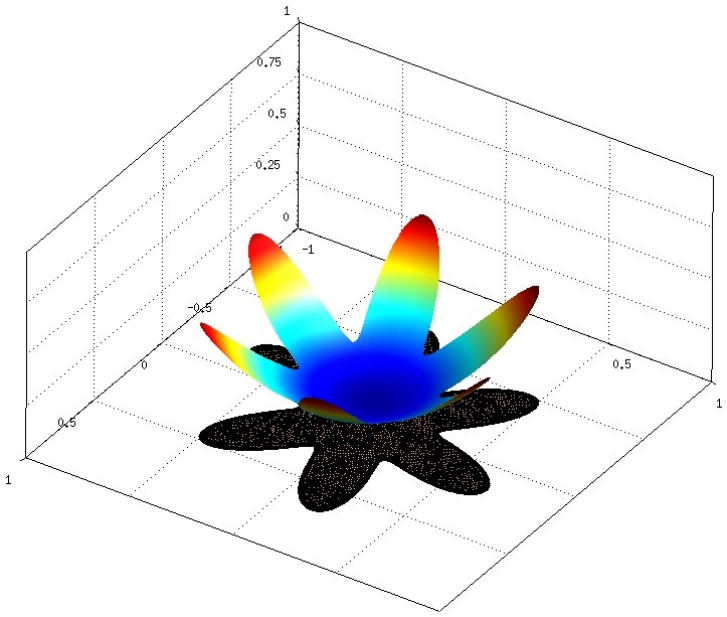

Figure 8: Three-dimensional view of solution for flower-like interface problem

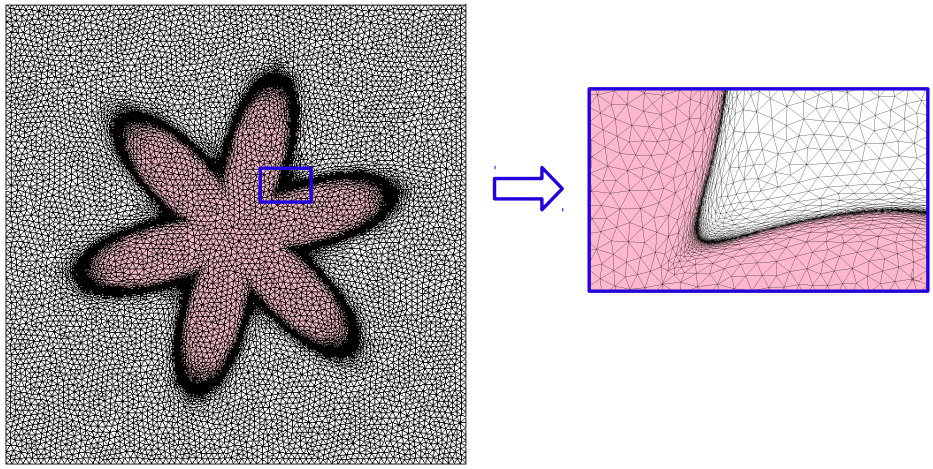

Figure 9: Computational domain and anisotropic elements in the vicinity of the level-set for the flower-like embedded interface problem: $p = 1, r = 2$ so that $r_\Gamma = 4$ and $r_t = 2$.

The error obtained for each sequence of meshes is plotted in Figure 10,

once again demonstrating the advantage of using anisotropic elements. The rate of convergence using uniform meshes is 1:1, whereas an optimal rate of convergence 1:2 is observed with anisotropic adaptive meshes. Besides this, while using anisotropic adaptive mesh increases accuracy of solution compared to isotropic mesh, the total number of mesh elements is nearly the same, as can be seen in Figure 11.

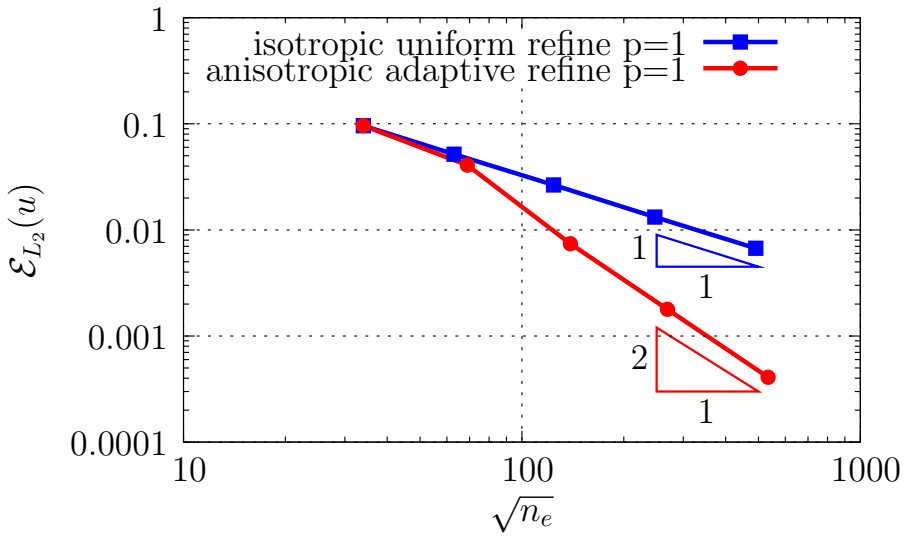

Figure 10: L_2 error norm for linear finite elements on isotropic uniform refined meshes and anisotropic adaptive refined meshes for the flower-like embedded interface problem ($p = 1, r = 2$).

Then, we use the anisotropic mesh sequence to solve the problem with finite elements of higher order $p = 2$ and $p = 3$. It can be seen from Equations (8) and (11) that the ratio $r_{n\Gamma}/r_t$ increases with p, so that the anisotropy of the mesh in the vicinity of the interface increases faster at higher order, while the elements remain isotropic in the bulk region. This allows the error to decrease uniformly in the domain with the optimal rate of convergence, i.e. third order for $p = 2$ and fourth order for $p = 3$, as shown in Figure 12. Figure 13 also presents optimal rate of convergence for solution error in L_∞ norm.

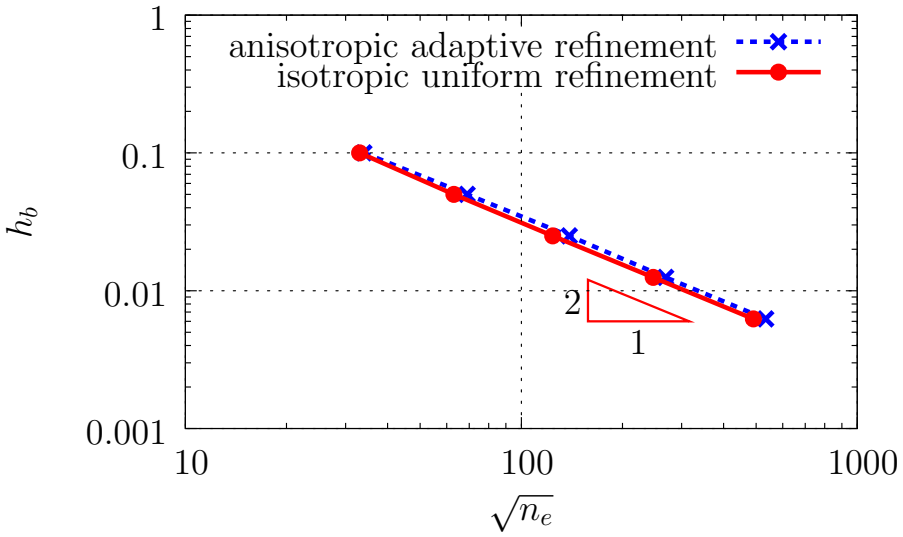

Figure 11: Total number of elements n_e against mesh size h_b in isotropic uniform refined and anisotropic adaptive refined meshes for the flower-like interface problem ($p = 1$, $r = 2$).

4. Spherical interface embedded in a cubic domain

In the previous section, we show the ability of our technique for a 2D problem. However, a broad range of industrial problems, such as the application in composite material science presented in Section 5, are inherently three dimensional.

In this section, we present a 3D example consisting of a spherical interface embedded in a cubic domain. A sphere Γ with radius $R = 0.41$ and center $(x_c, y_c, z_c) = (0.5, 0.5, 0.5)$ is described by the level-set function:

$$\phi(x, y, z) = \sqrt{(x - 0.5)^2 + (y - 0.5)^2 + (z - 0.5)^2} - 0.41 \tag{23}$$

The interface is embedded in the cube $\Omega = [0, 1] \times [0, 1] \times [0, 1]$ (see Figure 14(a)), where a Poisson problem outside the sphere is considered [21]:

$$\Delta u = 1/r^2, \qquad \text{in } \Omega \tag{24}$$

$$u = \log(R), \qquad \text{on } \Gamma \tag{25}$$

$$u = \log(r), \qquad \text{on } \partial\Omega \tag{26}$$

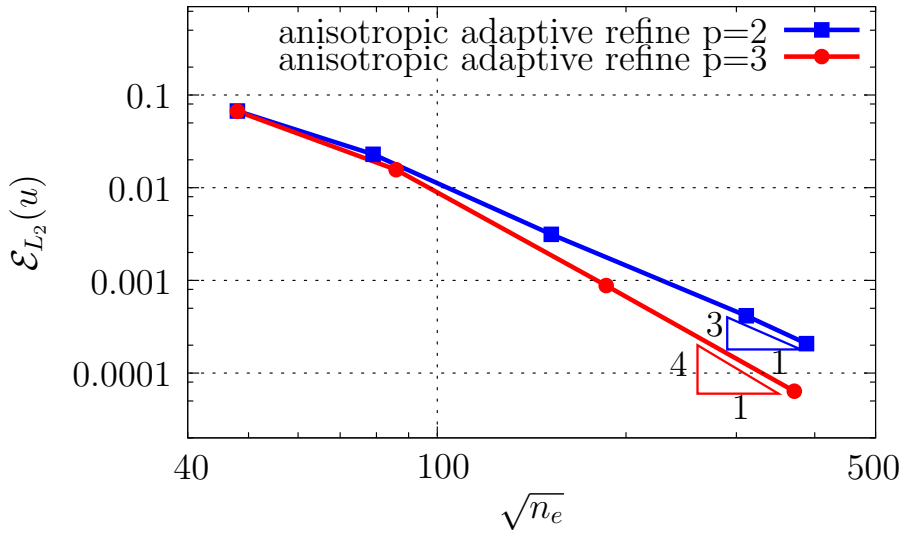

Figure 12: L_2 error norm for high-order finite element on anisotropic adaptive meshes ($p = 2, 3$), confirming optimal rate of convergence $\mathcal{O}(h^{p+1})$ up to 4^{th} order in flower-like interface case.

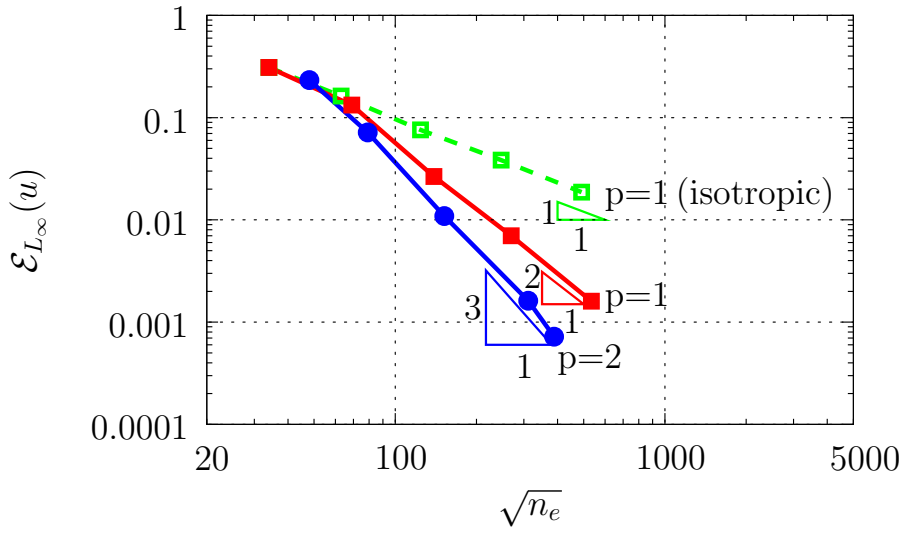

Figure 13: Solution error in L_∞ on isotropic uniform refined meshes ($p = 1$) and anisotropic adaptive refined meshes ($p = 1, 2$) for the flower-like interface problem.

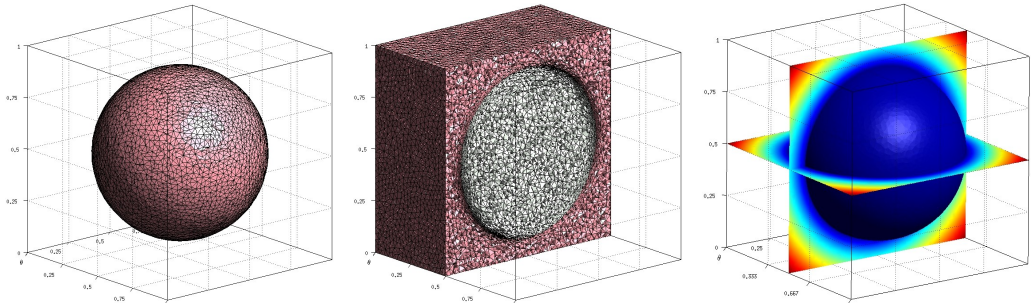

(a) Embedded sphere (b) Computational mesh (c) View of solution

Figure 14: Spherical embedded interface, computational anisotropic adaptive mesh and view of solution.

where $r = \sqrt{x^2 + y^2 + z^2}$, and is solved by a finite element method. The exact solution, that is symmetric about the center of the cube, is $u = \log(r)$. Dirichlet boundary condition imposed on the embedded interface Γ^* is determined by the exact solution, which is a constant function of sphere radius $u = \log(R)$.

Figure 14(a) shows the quasi smooth embedded sphere created by highly anisotropic adaptive mesh mesh elements which stretch along and capture well the interface as can be seen in Figure 14(b). Three dimensional view of finite element based solution is presented in Figure 14(c). L_2 errors of numerical solution and geometry obtained on four refined meshes are plotted in Figure 15. Geometry error in this case is defined as the distance of the embedded sphere Γ^* to the exact one Γ. Plot of convergence proves the second order of accuracy $\mathcal{O}(h^2)$ for the three dimensional case.

5. Applications

This part attempts to indicate possible applications of the proposed strategy in the field of fluid dynamics and material science.

5.1. Flow over cylinder

We first study laminar incompressible flow over a circular cylinder at low Reynolds number ($Re = 20$) using linear ($p = 1$) finite elements. We analyze two cases in which the embedded surface of the cylinder is approximated by locally isotropic and anisotropic adaptive mesh generation. The error in drag

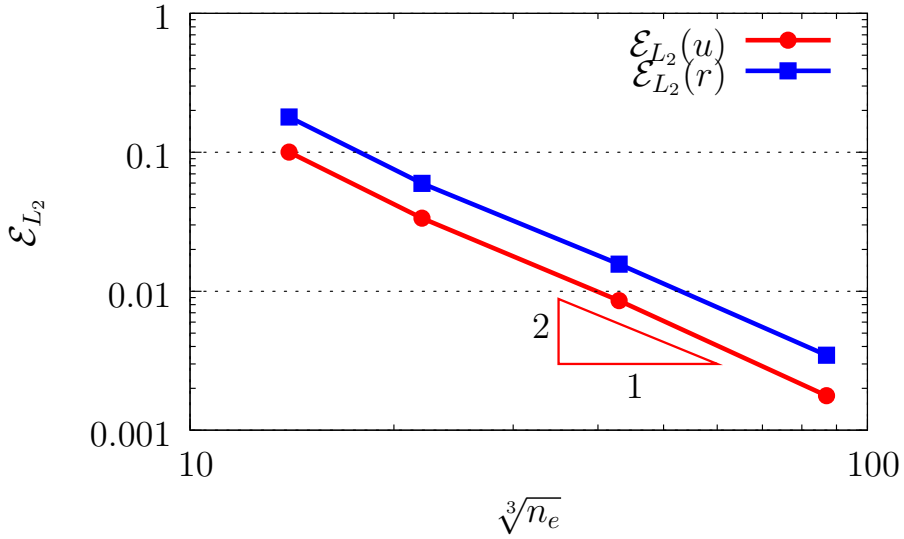

Figure 15: L_2 error norm was plotted for four anisotropic adaptive refined meshes, showing optimal rate of convergence $\mathcal{O}(h^2)$ in 3D spherical interface.

coefficient, as well as the geometry error defined as the difference between the length of the resulting embedded interface and the circumference of the exact circle, are calculated. Reference value for the drag coefficient is taken as $C_d = 2.13$ which is in the range listed in the literature [8, 9, 15, 31, 32, 33].

In order to investigate the influence of the geometry error on integral quantities computed over the approximated interface Γ^* (e.g. the drag coefficient), the uniform mesh size in the bulk region remains constant (i.e. $r_b = 1$) with $h_b = 0.16$, while mesh size in the vicinity of the interface undergoes adaptive refinement according to Eq. (21) with $r_{n\Gamma} = 2$ and $h^0_{n\Gamma} = 0.0016$.

It is clear that the isotropic adaptive refinement fails to predict the drag coefficient because of the large error in the approximation of the geometry. In addition, using very fine isotropic elements in the vicinity of Γ results in a very high number of elements, as can be seen in Tab. 2 and in Fig. 16. The convergence plot in Fig. 17 also shows that an appropriate local anisotropic mesh refinement leads the interface to converge towards the exact geometry, which decreases the resulting error in drag. Fig. 18 presents the solution obtained on the finest anisotropic adaptive mesh ($l = 3$).

l	h_b	$h_{n\Gamma}$	n_e^{aniso}	n_e^{iso}
0	0.16	0.0016	38067	56866
1	0.16	0.0004	40365	87171
2	0.16	0.0001	43897	138199
3	0.16	2.5e-05	45109	168907

Table 2: Flow over the cylinder at $Re = 20$. Mesh statistic for isotropic and anisotropic adaptive refinement.

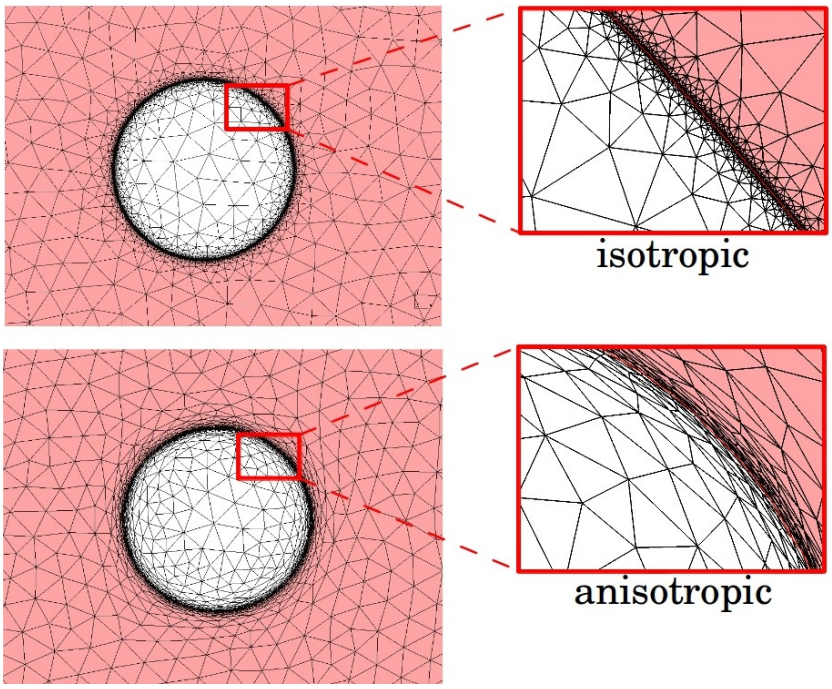

Figure 16: Flow over the cylinder at $Re = 20$. Isotropic and anisotropic adaptive mesh ($h_b = 0.16$, $h_{n\Gamma} = 2.5e\text{-}05$).

5.2. Two-phase flows

We consider a canonical problem of two phase flows: a circular bubble in static equilibrium. In this problem, the net surface force should be zero, since at each point on the bubble the tension force is counteracted by an equal and opposite force at a diametrically opposed point. We take as approach the

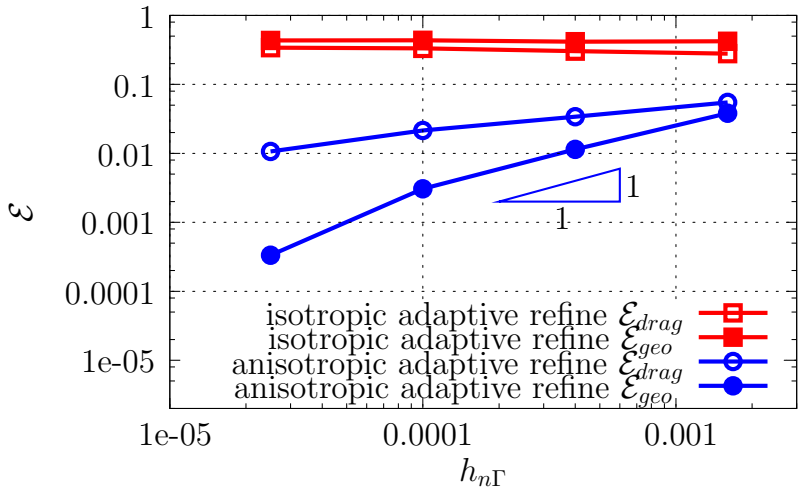

Figure 17: Convergence of geometry error and drag coefficient with isotropic and anisotropic adaptive mesh.

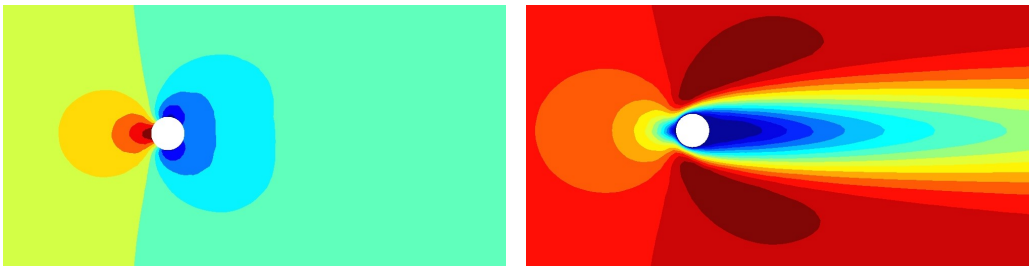

(a) Pressure field

(b) u-component of the velocity field

Figure 18: View of solution using anisotropic adaptive mesh ($h_b = 0.16$, $h_{n\Gamma} = 2.5e\text{-}05$).

Continuum Surface Force (CSF) method of Brackbill et al. [6], in which the surface tension force is given by:

$$\mathbf{f} = \gamma\kappa\mathbf{n}\delta^{\epsilon}_{\mathbf{\Gamma}},$$

where $\delta^{\epsilon}_{\Gamma}$ is a smoothed delta function with support on the bubble interface Γ, κ is the curvature of the bubble and γ is the surface tension coefficient (see Ref. [25] for more details).

The correct solution of the two-phase Navier-Stokes equations is a zero velocity field and a pressure field that rises from a constant value p_{out} outside the bubble to a value $p_{in} = p_{out} + \gamma/R$, where R is the radius of the bubble. The curvature κ can be computed exactly from the level set function of which the iso-zero value represents the fixed bubble. We assume a square domain of size $L = 4$ and a bubble of radius $R = 1$ centered at $(0, 0)$. We set $\gamma = 2$, the viscosity $\mu = 1$ and assume a ratio of density of $\rho_1/\rho_2 = 1000$.

The interface is replaced by a continuous transition region of which the thickness 2ϵ is of the order of mesh size. The width of the smeared region is chosen as $\epsilon = 1.5h_b$ for the isotropic mesh refinement and $\epsilon = 1.5h_{n\Gamma}$ for the anisotropic mesh refinement.

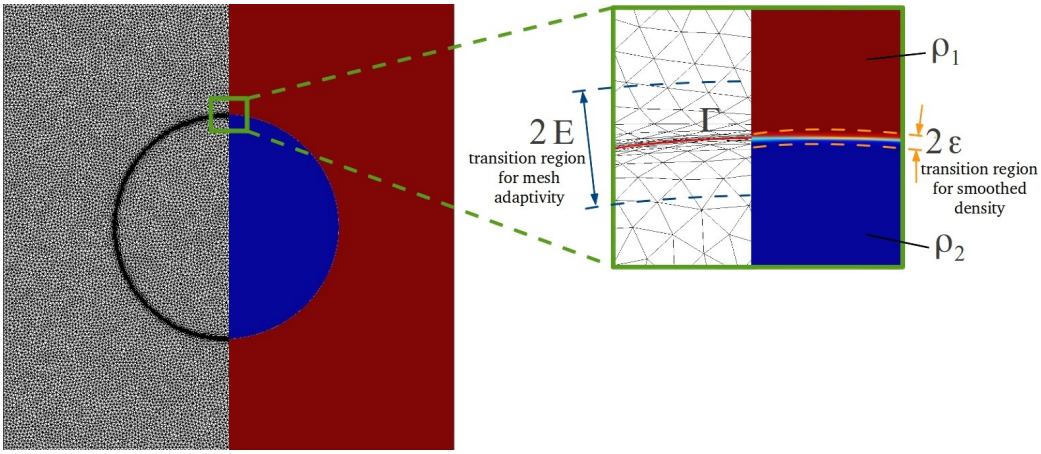

Figure 19: Illustration of transition region for mesh adaptivity and smoothed density in the neighbourhood of the interface Γ for anisotropic adaptive mesh ($l = 3$).

The density varies smoothly across the bubble interface by using a smoothed Heaviside function $H^\epsilon(\phi)$ of the signed distance ϕ to Γ:

$$H^\epsilon_\Gamma(\phi) = \begin{cases} 0 & \phi < -\epsilon \\ \frac{1}{2} + \frac{\phi}{2\epsilon} + \frac{1}{2\pi}\sin\left(\frac{\pi\phi}{\epsilon}\right) & -\epsilon < \phi < \epsilon \\ 1 & \phi > \epsilon \end{cases} \tag{27}$$

and the corresponding Dirac delta function is:

$$\delta_\Gamma^\epsilon(\phi) = \nabla H_\Gamma^\epsilon(\phi) = \begin{cases} 0 & \|\phi\| > \epsilon \\ \dfrac{1}{2\epsilon} + \dfrac{1}{2\epsilon}\cos\left(\dfrac{\pi\phi}{\epsilon}\right) & \|\phi\| \leq \epsilon \end{cases} \tag{28}$$

Solutions obtained on four consecutive isotropic uniform and anisotropic adaptive refined meshes ($l = 0, ..., 3$) are taken into consideration with initial mesh size ($l = 0$) set as $h_{n\Gamma}^0 = h_b^0 = L/15$. The relative error for the computed pressure drop can be estimated using Formulas (29),(30) given in Brackbill et al. [6] and Gerlach et al. [17], while the error in the spurious stream is measured by the maximal velocity in the computational field following Equation (31):

$$\mathcal{E}_{L_1}(\Delta p) = \left| \frac{\sum_{i=1}^{n_e^{in}} p_i - \gamma/R}{n e_e^{in}\,(\gamma/R)} \right|, \tag{29}$$

$$\mathcal{E}_{L_2}(\Delta p) = \left[\frac{\sum_{i=1}^{n_e^{in}} (p_i - \gamma/R)^2}{n_e^{in}\,(\gamma/R)^2} \right]^{1/2}, \tag{30}$$

$$\mathcal{E}_{L_\infty}(\|\mathbf{u}\|) = \max(\|\mathbf{u}\|), \tag{31}$$

where n_e^{in} is the number of mesh elements inside the bubble.

Figure 20 shows the plot of the pressure along the x-direction in the mid-section of the bubble. The pressure jump across the interface, as well a the constant pressure inside the bubble, can be observed. Convergence plots for the L_∞ norm of the spurious velocity $\|\mathbf{u}\|$) and the L_1 and L_2 norms for the pressure error (after 250 physical time steps $\Delta t_{phys} = d\mu/\gamma$) can be seen in Figure 21. It is clear that the isotropic mesh refinement strategy exhibits poor results for both velocity and pressure, whereas the anisotropic mesh strategy presented in this paper yields less spurious flows as the mesh is refined and successfuly recovers the rate of convergence for $\mathcal{E}_{L_\infty}(\|\mathbf{u}\|)$, $\mathcal{E}_{L_1}(\Delta p)$ and $\mathcal{E}_{L_2}(\Delta p)$. As expected, the convergence rates with anisotropic mesh refinement are always of one order higher than with isotropic meshes.

5.3. Composite material

A woven composite material in which the yarn surfaces are described by a level-set is taken into consideration.

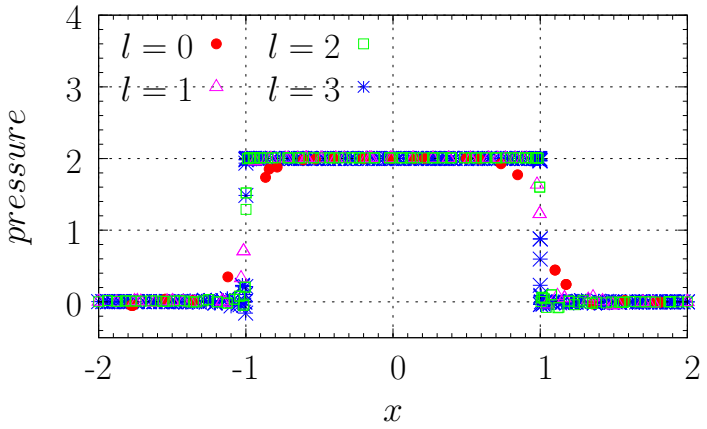

Figure 20: Computed pressure along x-direction at the mid-section ($y = 0$) of the bubble for different anisotropic adaptive refined mesh ($l = 0, ..., 3$).

The representative volume element of a woven composite is modeled. It is composed of cylindrical fibers with a sinusoidal axis organized perpendicularly with a phase difference to form a woven grid. Two layers of fibers are represented in the cubic cell. The geometry is inspired from the one studied in Reference [28] where XFEM is used to model complex geometries. The cube sides are equal to 2, the radius of the fibers is 0.1 and the sinus amplitude is 0.25.

Adapted meshes are created with the strategy presented in this paper, one analytical level-set representing each fiber surface. Three adapted meshes are produced, with varying elements size in the layer around the fibers surface. The normal element size $h_{n\Gamma}$ on the fiber surface and bulk element size h_b are changed to obtain finer meshes. The characteristic lengths of the meshes, as well as the resulting geometrical error $\mathcal{E}_{geo}$ on the surface of the fibers, are listed in Table 3. As expected, the geometrical error decreases with increasing mesh density (decreasing elements size around the surfaces). The finest mesh is shown in Figure 22(a).

A conformal mesh of high density is also created with a CAD modeler in order to compare the results of the adapted meshes (see Figure 22(b)). The geometry of the representative volume has been created using Spline curves to model the fibers. This conformal mesh is composed of 342078 tetrahedra.

The composite is submitted to loading test cases to determine its effective

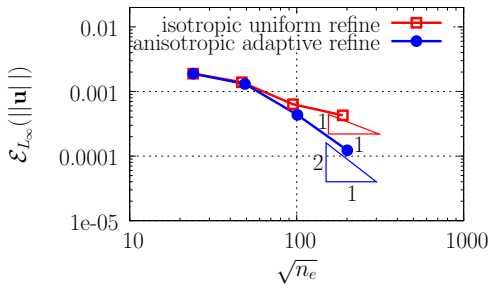

(a) Infinite error on the (spurious) velocity

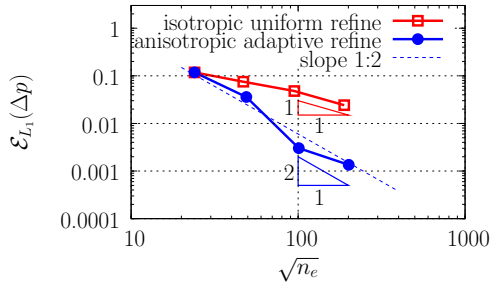

(b) L_1 error norm for pressure

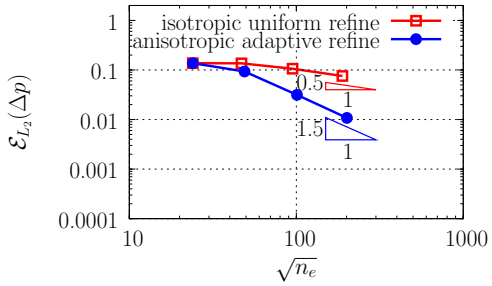

(c) L_2 error norm for pressure

Figure 21: Errors in velocity and pressure for the static bubble with a density ratio of $\rho_1/\rho_2 = 1000$.

h_b	$h_{n\Gamma}$	n_e	$\mathcal{E}_{geo}$ (%)
0.10	0.015	170588	10.60
0.08	0.010	273966	7.88
0.06	0.005	615564	3.70

Table 3: Mesh adaptation parameters and geometrical error for woven composite geometry.

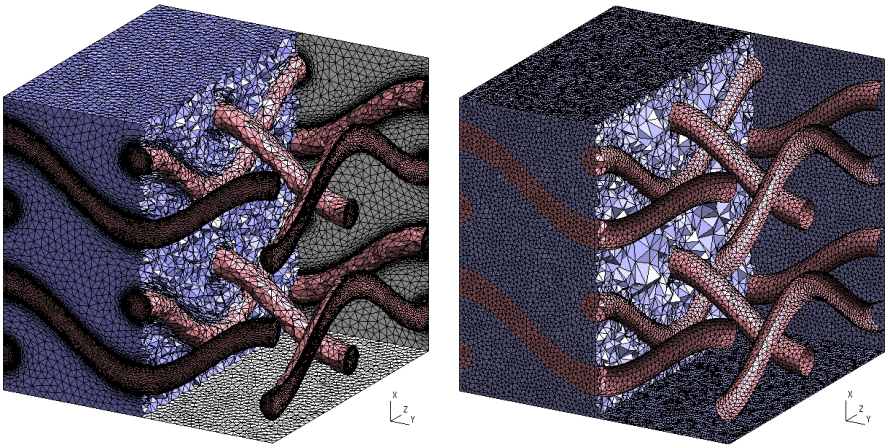

(a) Adapted mesh. (b) Conformal mesh.

Figure 22: Adapted and conformal meshes of woven composite.

stiffness. Boron fibers and an aluminum matrix are considered. The material properties are: $E_f = 400GPa$, $\nu_f = 0.3$, $E_m = 72GPa$ and $\nu_m = 0.33$. Two test cases are carried out. The first one is a tensile test case. The face $y = 0$ of the representative volume is fixed and a displacement of 1% of the side length is imposed in the y-direction on the opposite face ($y = 2$). This test enables to compute the effective elastic modulus of the composite in the y-direction. In the second test case, the face $y = 0$ is fixed and a displacement of 1% of the side length is imposed in the z-direction on the opposite face ($y = 2$). This test enables to determine the effective shear modulus in the yz-direction. First order finite elements are used to run these test cases.

The effective properties of the composite are obtained by integrating the stresses and the strains over the whole representative volume. The elastic modulus in the y-direction is obtained by the formula : $E_y = \frac{\bar{\sigma}_{yy}}{\bar{\epsilon}_{yy}}$, with $\bar{\sigma}_{yy}$ and $\bar{\epsilon}_{yy}$ being respectively the mean values of the stress and strain in the y-direction from the first test case. The shear modulus in the yz-direction is obtained by the formula $\mu_{yz} = \frac{\bar{\sigma}_{yz}}{2\bar{\epsilon}_{yz}}$, with $\bar{\sigma}_{yz}$ and $\bar{\epsilon}_{yz}$ being respectively the mean values of the stress and strain in the yz-direction from the second test case.

The conformal mesh gives an effective elasticity modulus of $82.2GPa$. It represents an increase of 14% compared to the matrix properties. The

effective shear modulus is $29.8GPa$, compared to $27.1GPa$ for the matrix. Figure 23 represents the normal stress distribution in the tensile test case along the y-axis with the finest adapted mesh. The relative error for the elasticity modulus and the shear modulus are computed for the 3 adapted meshes. The reference solution is calculated with a body-fitted mesh. The results are shown in Figure 24. The errors decrease as the adapted meshes contain more elements close to the surface of the fibers.

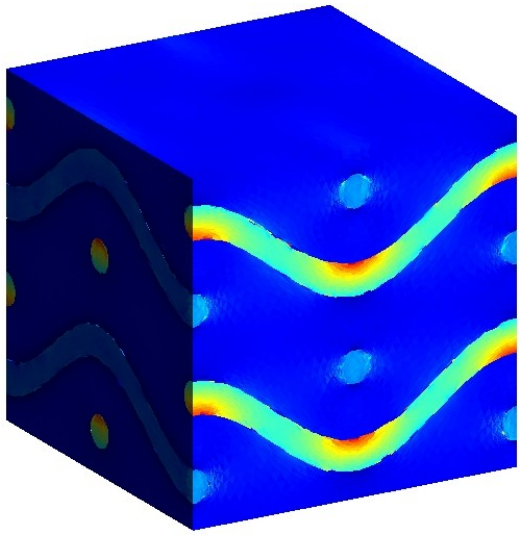

Figure 23: Tensile normal stresses in composite material with anisotropic adapted mesh.

This test case illustrates the effectiveness of the approach presented in this paper. The geometry is complex to model with a CAD modeler, while a level-set description is much simpler to set up. Moreover, the level-set description allows fibers to intersect. The adaptation procedure only requires the distance function resulting from the union of intersecting fibers. An example of such a mesh is shown in Figure 25.

6. Conclusion

An adaptive approach for modeling embedded surfaces is proposed and studied in detail in this paper. The geometry of the object under consideration is described by a level-set in the computational domain and the solution is calculated with a standard finite element method at various orders p. With

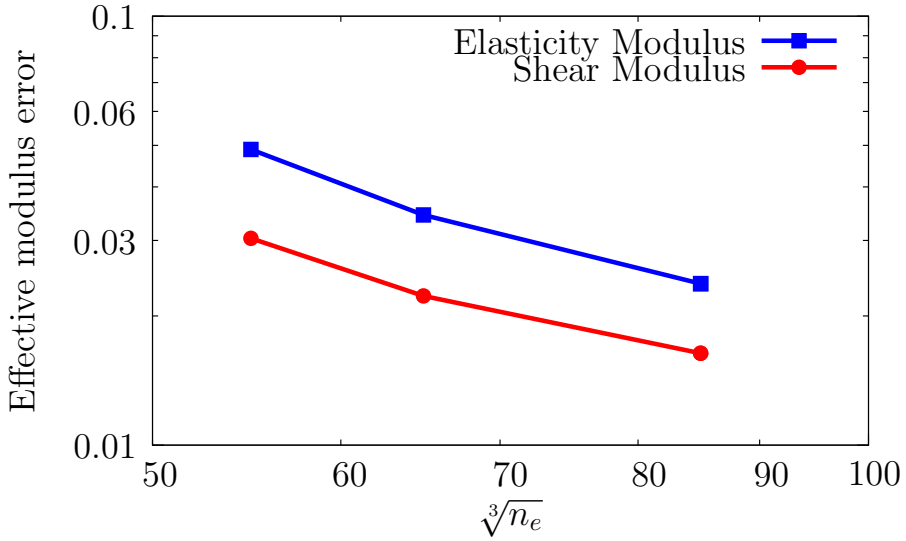

Figure 24: Composite material with local anisotropic meshes to describe the fibers : errors on effective moduli for tensile and shear test cases.

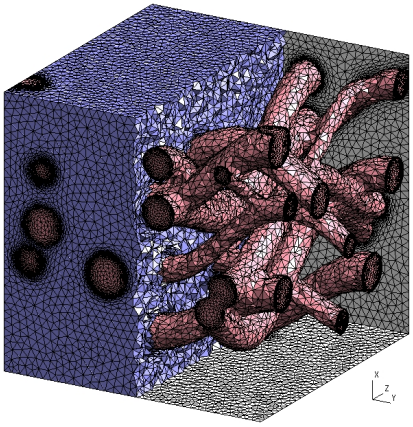

Figure 25: Adapted mesh of intersecting fibers composite.

uniform refinement, the large error that occurs on the embedded interface dominates the global solution over the computational domain; therefore, a faster local refinement near the interface is necessary to recover the optimal convergence rate.

The aim of this work is to propose a numerical approach that avoids the construction of conforming meshes for solving some relevant engineering analysis problems. We have demonstrated through the paper that the use of well chosen "nearly body-fitted meshes" allows to retrieve the optimal finite element convergence with barely the same number of degrees of freedom as for the conforming case.

Numerical examples involving irregular geometries in both two and three dimensions were performed, with excellent results. The geometrical error was also analyzed in detail to prove the advantage of the method when employing anisotropic elements to capture the complex geometrical features of the interfaces. Although anisotropically refined meshes exhibit a slight increase in the number of degree of freedoms (less than 20% in our proposed approach), they yield an optimal rate of convergence, whereas only first order accuracy is obtained from uniformly refined meshes.

The main advantage of our nearly body-fitted approach is that it does not interfere with the finite element solver: the final computation is done using standard finite element tools, without any change in the formulation. It is true, yet, that not all the computational mechanics community is already comfortable with the use of highly distorted/anisotropic meshes. Now that those meshing techniques are readily available, we strongly believe that, in a near future, anisotropic meshes will be used in a regular fashion.

References

[1] Volume of fluid (VOF) method for the dynamics of free boundaries. *Journal of Computational Physics*, 39(1):201 – 225, 1981.

[2] F. Alauzet. Metric-based anisotropic mesh adaptation, 2010. http://www-roc.inria.fr/gamma/Frederic.Alauzet/index.fr.html.

[3] Helio J.C. Barbosa and Thomas J.R. Hughes. The finite element method with lagrange multipliers on the boundary: circumventing the babuska-brezzi condition. *Computer Methods in Applied Mechanics and Engineering*, 85(1):109–128, 1991.

[4] E. Bechet, N. Moes, and B. Wohlmuth. A stable lagrange multiplier space for stiff interface conditions within the extended finite element method. *International Journal for Numerical Methods in Engineering*, 78(8):931–954, 2009.

[5] Pasko A.A. Belyaev A.G. and Kunii T.L. Ridges and ravines on implicit surfaces. In *Computer Graphics International 1998*, pages 530–535, 1998.

[6] J.U. Brackbill, D.B. Kothe, and C. Zemach. A continuum method for modeling surface tension. *Journal of Computational Physics*, 100:335–354, 1992.

[7] C. Bui, P. Frey, and B. Maury. A coupling strategy based on anisotropic mesh adaptation for solving two-fluid flows. *International Journal for Numerical Methods in Fluids*, 66(10):1226–1247, 2011.

[8] M. Coutanceau and R. Bouard. Experimental determination of the main features of the viscous flow in the wake of a circular cylinder in uniform translation. part 1, steady flow. *Journal of Fluid Mechanics*, 79(2):231–256, 1977.

[9] S.C.R. Dennis and G.-Z. Chang. Numerical solutions for steady flow past a circular cylinder at reynolds number up to 100. *Journal of Fluid Mechanics*, 42:471–489, 1970.

[10] C. Dobrzynski and P. Frey. Anisotropic Delaunay mesh adaptation for unsteady simulations. *Proceedings of the 17th International Meshing Roundtable*, pages 177–194, 2008.

[11] C. Dobrzynski, P. Frey, B. Mohammadi, and O. Pironneau. Fast and accurate simulations of air-cooled structures. *Computer Methods in Applied Mechanics and Engineering*, 195:3168–3180, 2006.

[12] C. Dobrzynski and P.J. Frey. Anisotropic Delaunay mesh adaptation for unsteady simulations. In *17th international Meshing Roundtable*, pages 177–194, 2008.

[13] J.E. Dolbow and L.P. Franca. Residual-free bubbles for embedded dirichlet problems. *Computer Methods in Applied Mechanics and Engineering*, 197:3751 – 3759, 2008.

[14] J.E. Dolbow and I. Harari. An efficient finite element method for embedded interface problems. *International Journal for Numerical Methods in Engineering*, 78(2):229–252, 2009.

[15] B. Fornberg. A numerical study of steady viscous flow past a circular cylinder. *Journal of Fluid Mechanics*, 98(4):819–855, 1980.

[16] P. J. Frey and P.-L. George. *Mesh Generation. Application to Finite Elements*. Hermès, Paris, 2000.

[17] D. Gerlach, G. Tomar, G. Biswas, and F. Durst. Comparison of volume-of-fluid methods for surface tension-dominant two-phase flows. *Internaltional Journal of Heat and Mass Transfer*, 49:740 – 754, 2006.

[18] F. Gibou, R.P. Fedkiw, L.T. Cheng, and M. Kang. A second-order-accurate symmetric discretization of the poisson equation on irregular domains. *Journal of Computational Physics*, 176(1):205–227, 2002.

[19] R. Goldman. Curvature formulas for implicit curves and surfaces. *Computer Aided Geometric Design*, 22(22):632–658, 2005.

[20] E. Hachem, T. Kloczko, H. Digonnet, and T. Coupez. Stabilized finite element solution to handle complex heat and fluid flows in industrial furnaces using the immersed volume method. *International Journal for Numerical Methods in Fluids*, 68(1):99–121, 2012.

[21] M. Hautefeuille, C. Annavarapu, and J.E. Dolbow. Robust imposition of dirichlet boundary conditions on embedded surfaces. *International Journal for Numerical Methods in Engineering*, 90(1):40–64, 2011.

[22] F. Hecht. Bamg: Bidimensional anisotropic mesh generator, 2006. http://www.freefem.org/ff++.

[23] Z. Li. A fast iterative algorithm for elliptic interface problems. *SIAM Journal on Numerical Analysis*, pages 230–254, 1998.

[24] E. Marchandise, G. Compère, M. Willemet, G. Bricteux, C. Geuzaine, and J.F. Remacle. Quality meshing based on STL triangulations for biomedical simulations. *International Journal for Numerical Methods in Biomedical Engineering*, 26(7):876–889, 2010.

[25] E. Marchandise, P. Geuzaine, N. Chevaugeon, and J.-F. Remacle. A stabilized finite element method using a discontinous level set approach for the computation of bubble dynamics. *Journal of Computational Physics*, 225(1):949–974, 2007.

[26] E. Marchandise and J.-F. Remacle. A stabilized finite element method using a discontinous level set approach for solving two phase incompressible flows. *Journal of Computational Physics*, 219(2):780–800, 2006.

[27] S. McKee, M.F. Tomé, V.G. Ferreira, J.A. Cuminato, A. Castelo, F.S. Sousa, and N. Mangiavacchi. The MAC method. *Computers & Fluids*, 37(8):907–930, 2008.

[28] N. Moës, M. Cloirec, P. Cartraud, and J.F. Remacle. A computational approach to handle complex microstructure geometries. *Computer Methods in Applied Mechanics and Engineering*, 192(28):3163–3177, 2003.

[29] N. Moës, J.E. Dolbow, and T. Belytschko. A finite element method for crack growth without remeshing. *International Journal for Numerical Methods in Engineering*, 43(1):131–150, 1999.

[30] C.S. Peskin. The immersed boundary method. *Acta numerica*, 11(1):479–517, 2002.

[31] D. Sucker and H. Brauer. Fluiddynamik bei quer angestroemten zylindern. *Waerme- und Stoffuebertragung*, 8:149–158, 1975.

[32] D.-J. Tritton. Experiments on the flow past a circular cylinder at low reynolds numbers. *Journal of Fluid Mechanics*, 6(4):547–567, 1959.

[33] C. Wieselsberger. New data on the laws of fluid resistance. *NACA TN 84*, 1922.